JOURNAL OF MATERIALS SCIENCE 30 (1995) 6209–6217

Thermal debinding of Fe_3Al–X metal powder compacts

I. MAJEWSKA-GLABUS, L. ZHUANG, R. VETTER, J. DUSZCZYK
Laboratory of Material Science, Delft University of Technology, Rotterdamseweg 137, 2628 AL Delft, The Netherlands

The process of removing a multicomponent binder from a metal powder compact has been investigated. Model experiments of debinding were performed on compounds consisting of less than 40 vol% binders (low molecular weight polyethylene, paraffin and *Carnauba* waxes) and more than 60 vol% metal content. As typical representatives for injection moulding morphology and meeting all other requirements for optimal powder characteristics, elemental powders of the Fe–Al system were used. Viscosity results over a wide range of shear rates for various plastisols are presented as functions of binder system composition and metal powder content. Based on the rheological response, an optimization of plastisol formulation was performed. Results are reported on three series of debinding modes using heat and fluid wicking in air and in nitrogen. The time dependence of fractional debinding, $x(t)$, during wicking has been estimated using a model. Direct observation by SEM of binder distribution and pore structure evolution at different stages of the debinding process was made. Wick-assisted thermal debinding in nitrogen proved to be an effective debinding method in terms of shape preservation and the absence of defects in the studied material.

1. Introduction

Metal Injection Moulding (MIM) is an interdisciplinary forming process aimed at combining the advantages of conventional powder metallurgy technologies with those of plastic injection moulding. It offers the advantage of producing large quantities of highly complex parts to net shape. For some time the process has been successfully applied to the manufacture of various ceramic components [1, 2]; more recently, injection moulding has been extended to metal [3] and cemented carbide systems. All versions of MIM consist of four steps: mixing, moulding, debinding and sintering, and all are based on the same principle as plastic injection moulding, except that the feedstock is an optimized mixture of very fine metal powder particles blended with a binder system. Volume ratios of powder to binder are typically around 60:40. After mixing, the homogeneous, plasticized mass can be injection moulded. However, once the moulding process has been completed, the binder must be eliminated. This step, called debinding has proved to be the most difficult and time-consuming stage of the MIM process. It can be accomplished using a variety of techniques, including solvent extraction, wicking, and thermal decomposition [4–7].

This paper discusses thermal debinding specifically, as applied to an optimized model composition consisting of a multicomponent binder and an elemental powder system (Fe_3Al–X intermetallics [8], where X is Cr, Ni, B) as being typical for injection-moulding morphology (sizes, size distributions, specific surface areas, etc) [9, 10]. Because powder characteristics directly influence the debinding process [9, 10], the results obtained in this work might be extrapolated to other systems with similar morphology.

2. Experimental procedure

2.1. Materials

Debinding experiments were performed with cylindrical samples obtained by warm pressing a homogeneous mixture of an optimized plastisol formulation containing 63 vol% elemental metal powders and 37 vol% binders. The optimization was based on rheological characteristics.

2.1.1. Metal powders

The solid state used throughout the course of this research was a mixture of iron–aluminium elemental metal powders. The composition was chosen to be close to Fe_3Al intermetallic compound. Additives such as nickel, boron and chromium, were applied for better alloy design [8] and in order to improve packing density, angle of repose (boron, chromium) and to avoid slumping during debinding (nickel, with its non-spherical shape) [9]. Atomic and weight percentages of the blend are given in Table I.

Tap and apparent densities were 52% and 41%, respectively. The angle of repose was improved by additives from 44° to 49°.

0022–2461

TABLE I Metal powder mixtures used

	Fe	Al	Ni	B	Cr
(at%)	75	20	2	1	2
Atomic mass ($g\,mol^{-1}$)	55.85	26.98	58.69	10.81	52
(wt%)	84.41	10.87	2.36	0.22	2.14

TABLE II Results of particle-size analysis and specific surface area measurements. d (50%) is the particle size at 50% weight; d_{vm} is the volume mean diameter, the diameter of a sphere with equal volume; d_{vs} is Sauter mean diameter, the diameter of a sphere with equal surface area per unit volume; S_m is the measured specific surface area

	d (50%) (μm)	d_{vm} (μm)	d_{vs} (μm)	S_m ($m^2\,g^{-1}$)	Particle shape
Fe	8.0	9.5	7.0	0.3158	Spherical
Al	7.7	9.3	6.4	0.6435	Spherical

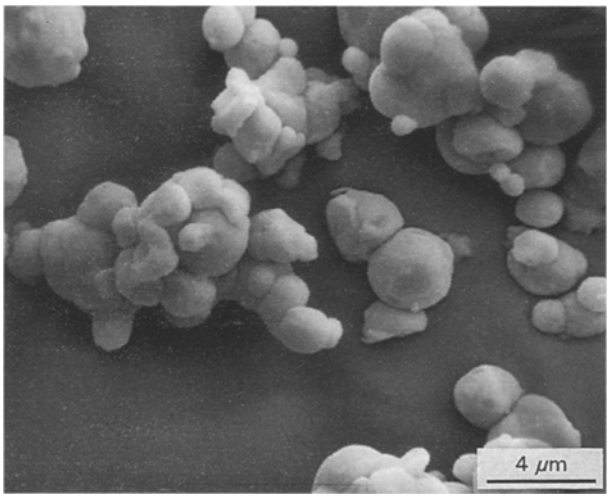

Figure 1 Scanning electron micrograph of iron powder.

Powder characteristics, considered to have influential effect on the debinding process, were measured. These include particle-size distribution (using a Malvern particle sizer), specific surface area (determined by BET method), and metal powder shapes (by scanning electron microscopy studies). Measured and calculated results of particle-size analysis and specific surface area are presented in Table II; scanning electron micrographs of iron and aluminium are shown in Figs 1 and 2 and plots of cumulative weight against particle size for iron and aluminium are given in Figs 3 and 4, respectively.

Although the particle characteristics needed for an ideal processing lead to some conflict between requirements of the individual stages, an optimum can be found for MIM powder [9]. The most important requirements concern sphericity of particle shape, small mean particle size, considerable size distribution, sufficient interparticle friction to avoid slumping and a clean particle surface [9, 10]. Morphology data presented above, in Table II and in Figs 1–4, indicate that metal powders applied in this work meet all these requirements, and therefore can be treated as a model system for investigation of debinding.

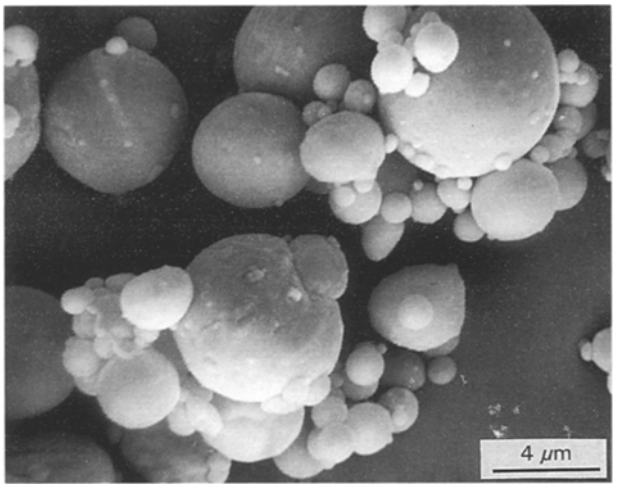

Figure 2 Scanning electron micrograph of aluminium powder.

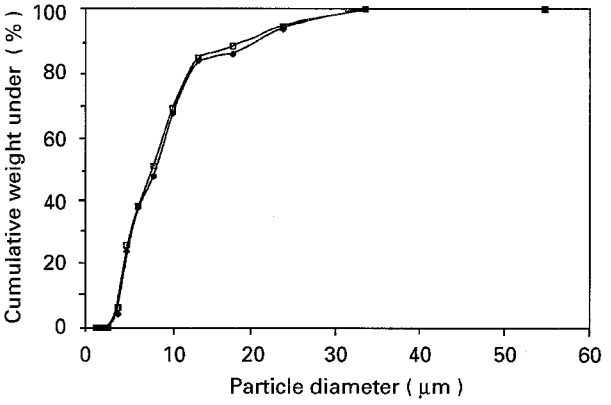

Figure 3 Distribution of particle sizes in iron powder determined using a Malvern particle sizer.

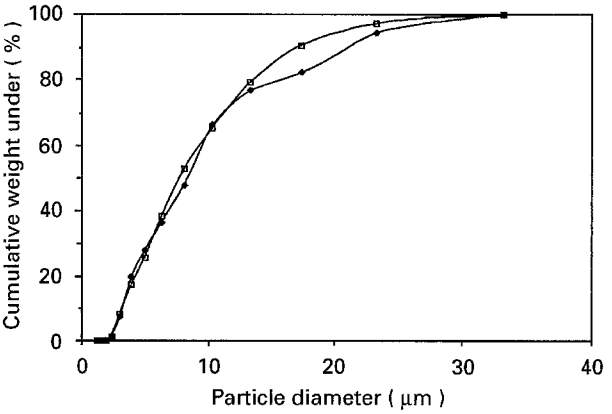

Figure 4 Distribution of particle sizes in aluminium powder determined using a Malvern particle sizer.

TABLE III Oxygen and hydrogen content in iron and aluminium powders

	Fe	Al
Oxygen (wt%)	0.19	0.28
Hydrogen (p.p.m.)	9.0	24.5

The oxygen and hydrogen content in the aluminium and iron powders under investigation were also measured. The results are presented in Table III. The oxygen content was established by infrared (IR) analysis using a Stroehlein OSA–MAT analyser. The hydrogen

TABLE IV The melting and viscosity characteristics of binder constituents

Material	Density (10^6 g m^{-3})	Melt temp. (°C)	Activation energy (kJ mol^{-1}) [14]	Viscosity at ref. temp. (Pa s)	Reference temp. (°C)
Paraffin wax	0.90	61	4.4	0.009 [15]	101
Carnauba wax	0.97	85	12.3	0.021 [15]	111
Polyethylene	0.92	114	33.0	290.0	119

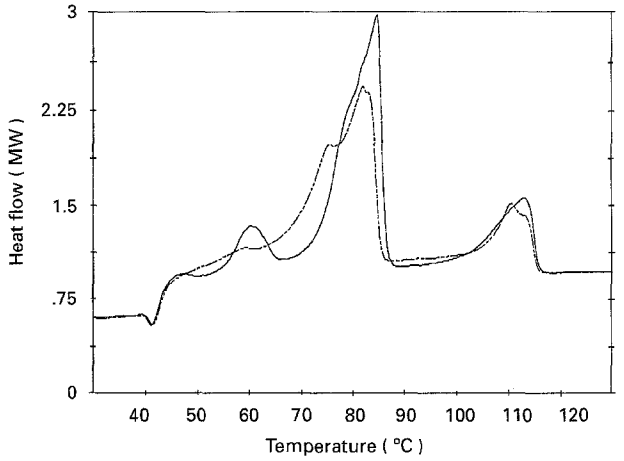

Figure 5 DSC data on the heat flow versus temperature for multi-component binder (—) before (Mix 1) and (- - -) after (Mix 2) mixing.

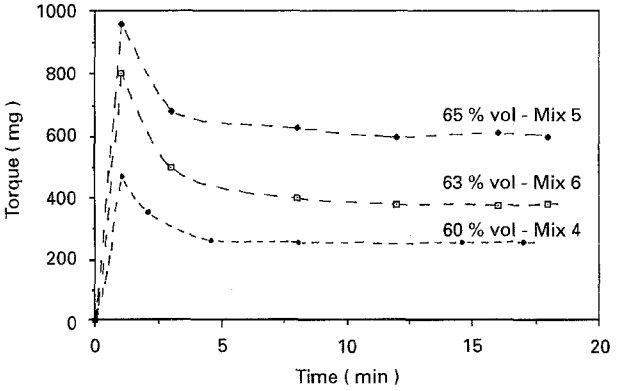

Figure 6 A typical Brabender Plastograph torque–time plot recorded during mixing binders with different volume loadings of metal powders.

content was measured by means of an H-MAT Strohlein gas analyser using a standard procedure [11]. The very large content of the hydrogen in aluminium powder should be noticed: 25 p.p.m. hydrogen is approximately equal to 28×10^{-6} m^3 H_2 per 100 g powder, which is more than 100 times larger than the industrial limit for ingot aluminium [11].

2.1.2. Binders

The primary binder system used in this study was composed of low molecular weight polyethylene, paraffin and *Carnauba* waxes. As in prior works [12, 13] the low molecular weight polyethylene was selected as a backbone material, to give the binder green strength and strength in the transition between debinding and sintering. Paraffin wax was chosen for its wide range of molecular size and was used to give the mixture a low viscosity. *Carnauba* wax, a natural wax formed on Brazilian palm leaves, was chosen because of its hardness and low melting temperature which varies between 80 and 87 °C. In addition it acts as both a lubricant and an internal mould release. The melting and viscosity characteristics of binder constituents are given in Table IV. Fig. 5 shows the differential scanning calorimeter (DSC) pattern of this binder before and after mixing for scanning rate of 10° min^{-1}. The melting temperatures of the respective binder components shift by few degrees towards lower temperatures as the components are mixed together.

2.1.3. Wicking powder

Four different wicking powders were applied: three silicon carbide (SiC) powders with an average particle size of 0.8, 3.0 and 9.3 μm, and one aluminium oxide powder of 0.013 μm.

2.2. Procedure of plastisol optimization

2.2.1. Mixing

In order to prepare samples for debinding experiments, elemental powders were blended for 24 h in a Turbula P2C mill prior to mixing with binders under high shear conditions in a Brabender plastograph at 135 °C. During mixing, torque–time plots were recorded. Fig. 6 illustrates these plots registered for plastisols containing different powder loadings. Mixing was considered to be fully completed when the measured torque reached a steady constant minimum.

2.2.2. Rheology

The aim of this part of the research was to establish the rheological behaviour of plastisol formulations as a base for subsequent selection of a suitable candidate for further processing. The criterion of this suitability was the ease of mixture flow into a die cavity which, in turn, was monitored by the viscosity measurements.

Rheological characteristics of plastisol formulations presented in Table V were determined using the Instron 3211 Capillary Rheometer. Apparent viscosities were evaluated over a wide range of shear rates 7–2000 s^{-1}.

The selection was based on the two-stage investigation process: first, the optimization of the binder composition with fixed (at 60 vol %) metal powder content (four mixes); second, the optimization of the volume loading of metal powders with fixed (chosen in the first step) binder system (two mixes). Fig. 7 shows the results of the first stage of the process – the effect of different binder composition (see Table V for plastisol

TABLE V Plastisol formulations used in the course of this research

Mixture number	Powder (vol%)	Binder composition (vol%)		
		Polyethylene	*Carnauba* wax	Paraffin wax
Mix 1	60.0	13.3	13.3	13.3
Mix 2	60.0	15.0	20.0	5.0
Mix 3	60.0	20.0	15.0	5.0
Mix 4	60.0	17.5	17.5	5.0
Mix 5	65.0	15.3	15.3	4.4
Mix 6	63.0	16.19	16.19	4.62

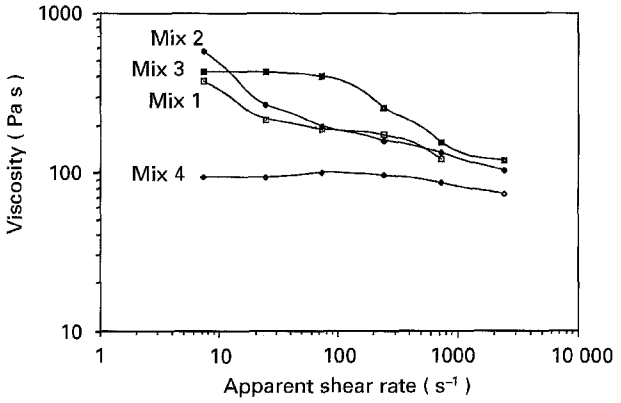

Figure 7 Flow curves showing the effect of different binders at 135 °C.

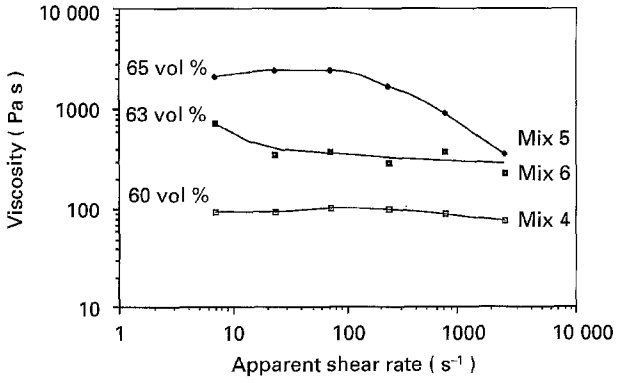

Figure 8 Flow curves showing the effect of metal powder volume fraction at 135 °C.

formulations). Fig. 8 presents the results of the second stage, where viscosities of plastisols are displayed as a function of volume loading of metal powders.

Based on acquired viscosity data, the selection was made of a plastisol containing 63 vol % metal powder at room temperature (Mix 6).

2.2.3. Compacting

After mixing, the feedstock was hot pressed into cylinders of 25.4 mm diameter and four thicknesses (4, 6, 8 and 12 mm). Samples were then treated in a furnace under various time–temperature conditions in either air or nitrogen and in either the presence or absence of wicking powder. The amount of binder removed was assessed by measuring the weight loss after treatment. Usually three specimens were incorporated in each debinding cycle.

2.2.4. SEM

For direct observation of binder distribution and pore structure evolution, a scanning electron microscope was used. In order to avoid the local heating and charging effect of polymeric binders, samples were sputtered with gold and well grounded to the sample holder prior to examination. The applied energy of the electron beam was 25 keV.

3. Results and discussion

The debinding process was investigated by sets of experiments of three types:

1. thermal debinding in both air and nitrogen at 450 °C;
2. wick-assisted debinding at temperatures from 70–175 °C with isothermal holds for 1, 2, 4, 8 and 65 h in different wick powders;
3. combined wick and thermal debinding with cycles of constant heating rates and isothermal holds.

Temperature profiles for these three debinding modes are presented in Fig. 9.

As part of a preliminary research, the requirements for debinding by thermal degradation have been investigated by thermogravimetric and differential thermogravimetric analysis (TGA and DTGA). This has been carried out with a heating rate of 10 °C min^{-1} in a nitrogen atmosphere on samples of mixed plastisols after rheology tests. TGA and DTGA profiles are illustrated in Figs 10 and 11, respectively. The decomposition temperature range for the studied binder system is between 300 and 570 °C with the highest rates of weight loss at about 500 and 550 °C. Fig. 10 shows clearly that above 570 °C, all 100% of the binder available for debinding (i.e. 7.86 wt% mixed plastisol) undergoes complete pyrolysis without leaving any residue. However, these TGA data must be treated as an indication of temperature ranges only, because every change in part weight, shape or thickness influences the results of the analysis very strongly. On the other hand, DTGA data are most helpful when a heating schedule for debinding is planned: the

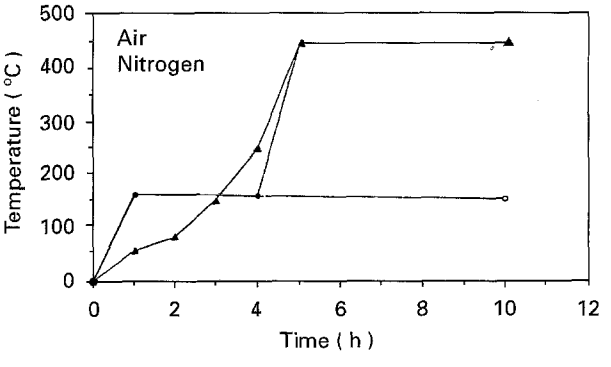

Figure 9 Debinding modes. (▲) thermal, (●) wick + thermal, (○) wick.

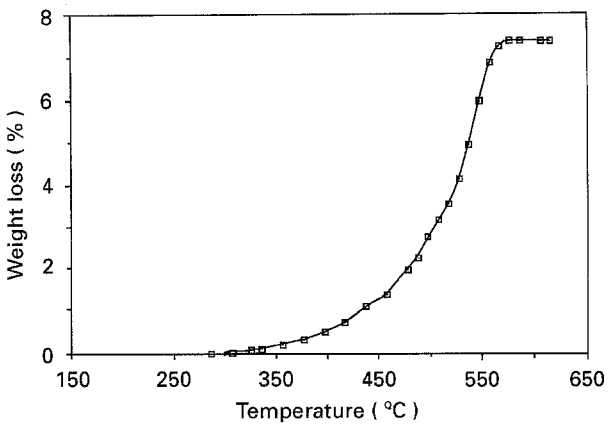

Figure 10 TGA curve for Mix 6 showing binder volatilization at a constant heating rate of 10 °C min^{-1}.

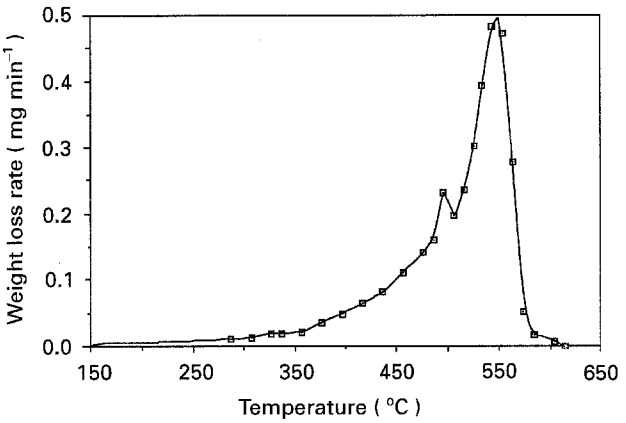

Figure 11 DTGA curve for Mix 6 showing binder volatilization rate at a constant heating rate of 10 °C min^{-1}.

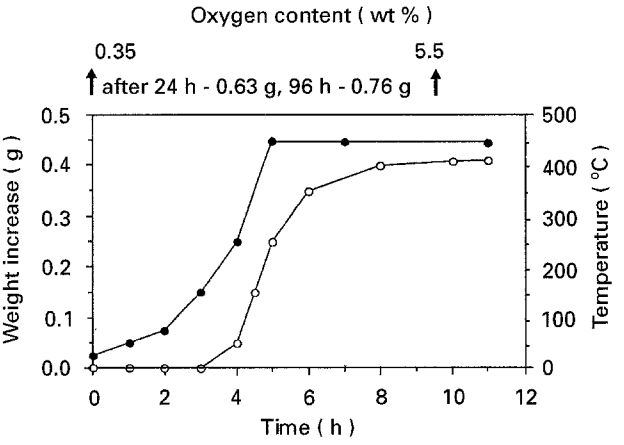

Figure 12 Thermal debinding in air: (○) weight increase, and (●) temperature as a function of time.

weight-loss rate curve gives critical temperatures of debinding. Putting some dwell times to these areas can prevent too rapid a binder removal.

3.1. Thermal debinding

Fig. 12 illustrates the process of thermal debinding in air. The change in specimen weight (on the left-hand side) is shown together with the temperature profile of the process (on the right-hand side) versus debinding time. The sample after treatment exhibited visible defects on the surface of the part: shape distortion, discoloration,

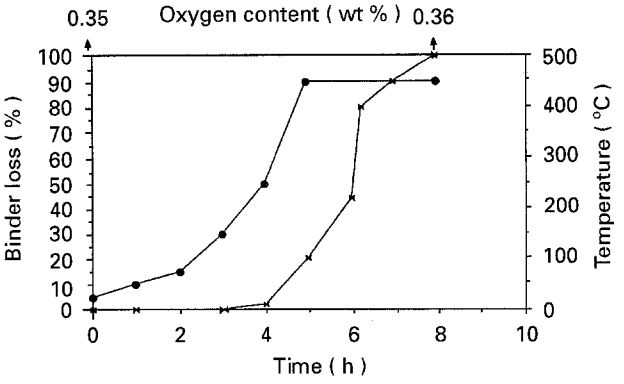

Figure 13 Thermal debinding in nitrogen: (⋈) binder loss, and (●) temperature as a function of time.

blisters and cracks. This is consistent with the results presented in Fig. 12, where only an increase in weight is observed. Fig. 12 also presents some results of analysis for the oxygen content in the investigated material at various stages of the debinding process. It exhibits a considerable increase from 0.35 wt% to 5.5 wt%. This was not the case with the carbon content, which was measured for the pure blend of elemental powders as 0.88 wt%; at the beginning of the debinding (with 100% binders) it was 5.59 wt% and at the end of the process it was 0.90 wt%.These results confirm the conclusion that the measured weight increase is due to the metal oxidation taking place if the debinding process proceeds in the absence of a protective atmosphere.

Fig. 13 presents the results of thermal debinding in a nitrogen atmosphere. The amount of binder loss and the temperature programme are plotted versus debinding time. The amount of binder loss is expressed as a percentage of the total binder weight that is available for debinding. The temperature is programmed as given previously. The process of weight decrease becomes measurable after approximately 3 h when the temperature exceeds 150 °C, and then proceeds relatively quickly with the temperature still rising up to 450 °C. All 100% binder is removed after approximately 8 h. After 6 h debinding, when about 80% of the binder was extracted, the part was not fragile, while the fully debound one was so brittle that it could not stand any handling. Moreover, in Fig. 13 results of the oxygen analysis are marked at the beginning and end of the process. They imply that the increase of oxygen content in the material debound in a protective atmosphere of nitrogen is insignificant.

3.2. Wick debinding

In order to investigate the influence of the wick powder type and size on the rate of the binder removal, four different wick powders were applied: three silicon carbide (SiC) powders with average particle sizes of 0.8, 3.0 and 9.3 μm and one aluminium oxide powder of 0.013 μm. The results are presented in Table VI. It is seen that any detectable debinding effect can be observed only when the finest wick powders – SiC of 0.8 μm and Al_2O_3–C of 0.013 μm – are used [16]. Because the capillary attraction by the wick increases

TABLE VI Debinding in different wick powders

Binder loss after 65 h (%)	SiC			Al_2O_3–C, 0.013 μm
	F600–9.3 μm	F1200–3μm	UF15–0.8 μm	
120 °C	0	0	23	–
130 °C	–	–	–	36
145 °C	0	0	40	–

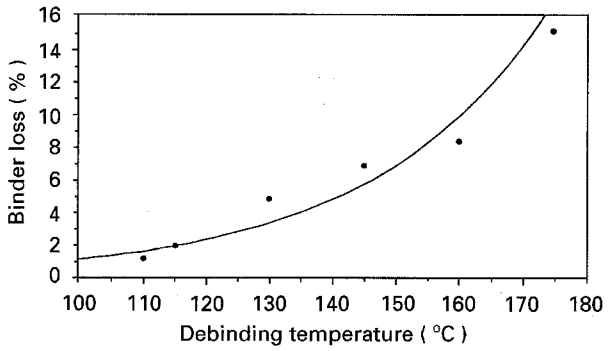

Figure 14 The amount of binder lost after 2 h debinding in SiC UF 15 wick powder.

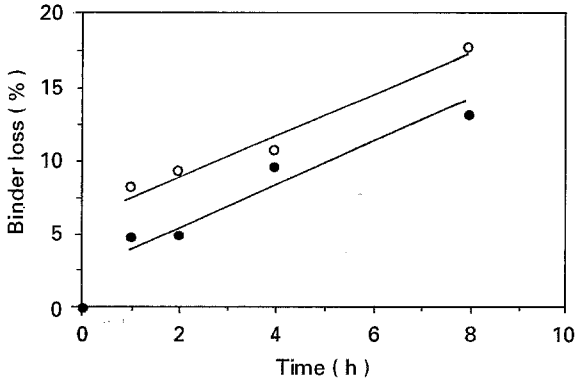

Figure 15 The amount of binder lost during debinding in SiC (0.8 μm) wick powder at (●) 130 and (○) 160 °C: after 400 h, 45% binder was lost.

with decreasing inter-pore radius in the wick powder, no binder is absorbed if the wick powder granules are too coarse to provide sufficient sample-to-wick contact area.

Figs 14–16 present results of wick-assisted debinding in SiC U15 powder with average particle diameter of 0.8 μm. The time and temperature dependence of the debinding process is illustrated in Figs 14 and 15. Fig. 14 plots percentage of binder extracted in 2 h versus various hold temperatures from 100–175 °C. At low temperatures, only the waxes are mobile enough for wicking extraction. For temperatures over approximately 120 °C, all binder components are molten and the process accelerates exponentially, as shown in Fig. 14. Fig. 15 shows plots of the amount of binder loss versus debinding time at 130 and 160 °C. The percentage of binder removed after 8 h is approximately 13% and 18% for the lower and higher debinding temperatures, respectively. Leaving the part at

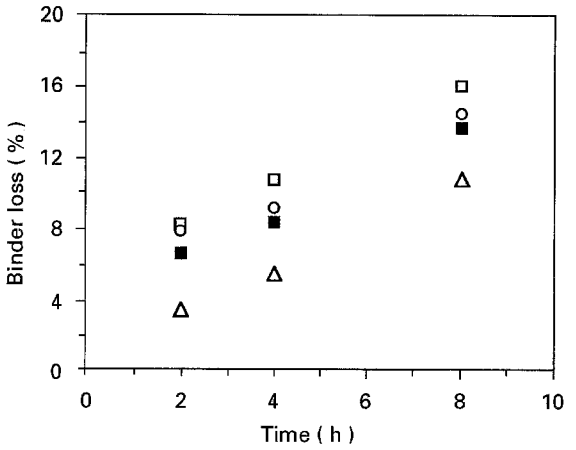

Figure 16 The effect of specimen height on the debinding process at 160 °C in SiC UF 15 wick powder: (□) 4 mm, (○) 6 mm, (■) 8 mm, (△) 12 mm.

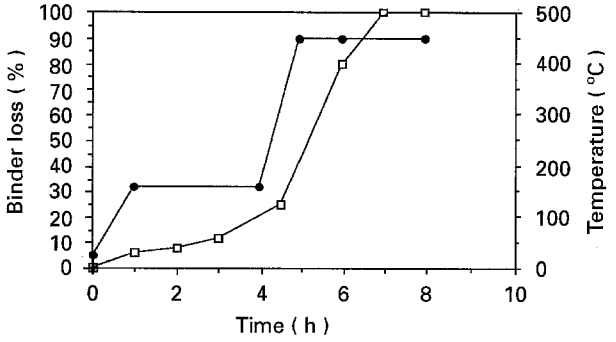

Figure 17 Wick-assisted thermal debinding in nitrogen: (□) binder loss, (●) temperature.

160 °C for 400 h resulted in only 45% binder removal. Parts after these experiments were very easy to handle and without any detectable defects.

Fig. 16 shows the effect of the specimen thickness on debinding process. The percentage of binder loss is plotted versus debinding time for compacts in four thicknesses: 4, 6, 8 and 12 mm. After 8 h at 160 °C in SiC U15 powder, a maximum of 18%, 13%, 10% and 8% of the binder was extracted from 4, 6, 8 and 12 mm high samples, respectively. The percentage of binder loss exhibits linear dependence on the debinding time for all four thicknesses.

An attempt was made to estimate the debinding time in the wicking process. German [17] developed a theoretical model by which the total time of debinding, t_1, can be evaluated. In order to calculate the time dependence of the fractional debinding, $x(t)$, expressed in Figs 13–17 as "% binder loss", we have extended this model [18] by:

1. incorporation of the packed bed resistance, (the result of the wick powder presence);
2. introduction of the hydraulic diameter of the pores, $(2/3)DE/(1 - E)$, where D is the particle diameter, and E is the porosity in the expression for the capillary pressure.

The influence of the wick powder permeability modifies the second part of the $x(t)$ curve. A linear approximation of the first part yields the following

equation for the debinding rate

$$\frac{dx}{dt} = \frac{\gamma \cos \Theta E_C^2 D_C}{15H^2 \eta (1 - E_C)} \times \left\{ \frac{D_C E_C (1 - E_W)}{D_W E_W (1 - E_C)} - 1 \right\} \quad (1)$$

where γ is the surface tension of the binder, Θ the contact angle between wick and compact, H the sample height, η the viscosity of the binder, E_C the relative porosity of the compact, E_W the relative porosity of the wick, D_C the average particle size of the compact, and D_W the average particle size of the wick. The sign of the last factor of Equation 1 indicates that the wicking action is expected to occur if the hydraulic diameter of the compact pores exceeds that of the wick powder. The result is capillary flow from compact to wick.

Using Equation 1 the theoretical debinding rate was calculated for $T = 160\,^{\circ}C$, $H = 4 \times 10^{-3}$ m, $\eta = 0.67$ Pa s at 160 °C, $E_C = 0.37$, $E_W = 0.7$, $D_C = 6 \times 10^{-6}$ m, $D_W = 0.8 \times 10^{-6}$ m, γ was estimated to be of the order of 0.05 N m^{-1} and the cosine of Θ was assumed to be unity (experimental data were not available). The temperature of 160 °C was chosen in order to allow a comparison of the calculated theoretical value of the debinding rate ($dx/dt = 3.4 \times 10^{-4}$ s^{-1}) with experimental values presented in Figs 15 and 17 where the first isothermal hold for 3 h was made at 160 °C. After 3 h at 160 °C, 10%–15% of binder was removed, as shown in Figs 15 and 17, respectively. The differences in measured $x(t)$ values from 10%–15% are due to the different heating rates applied in both cases: 9 °C min^{-1} corresponds to 10% and 2.2 °C min^{-1} to 15%. However, a large discrepancy of a factor of 40 between calculated and measured results still remains, although the gap with Germans' model [17] has been slightly narrowed by some refinements. Because of the quadratic dependence of x on t, dx/dt is equal to $1/2t_1$ rather than to $1/t_1$. With introduction of the hydraulic pore diameter, the theoretical rate (depending on the experimental conditions) is further lowered, by a factor of 7 in the present case. Additional reduction might be expected from non-zero values of the contact angle and from ineffectiveness of part of the pore channels caused by holes blocking the transition from compact to wick. Other modifications, which should account for the observed discrepancy between experimental results and this model for wick debinding, are presently under investigation.

3.3. Wick-assisted thermal debinding

The binder removal cycle in a nitrogen atmosphere and in the presence of SiC U15 wick powder, is presented in Fig. 17. The amount of binder loss and temperature programme are plotted versus debinding time. The temperature programme consists of a combination of constant heating rates with two isothermal holds at 160 and 450 °C. After approximately 7 h 100% binder is removed. In the first 4 h the process of debinding proceeds very slowly, extracting about 20% of the binders. After the rapid rise in temperature to 450 °C the process accelerates, and the removal of the remaining 80% binders is completed within the next 3 h. No defects were observed in the fully debound part and the shape was retained without distortions.

3.4. SEM observations

Direct observations by SEM were made on binder distribution and pore structure evolution during wick-assisted thermal debinding in nitrogen (see, for reference, Fig. 17). Different areas of the centre regions of fractured samples were examined at the beginning and at two intermediate stages of the process: with 25% and 80% of binders removed. Figs 18 and 19 show the morphology of these areas in the as-received sample. It is fully filled with binder. Figs 20 and 21 demonstrate the centre region of the sample after 4.5 h debinding, when 25% of the binder is removed. Here binders and particles form discrete islands of agglomerates. Fig. 20 shows an area of the fractured sample where most regions are filled with binder. This is most likely caused by the outward flow of the binder from the centre region because of the pressure build up from the internal decomposed gas. However, more significantly, a small pore channel can be observed in Fig. 20,

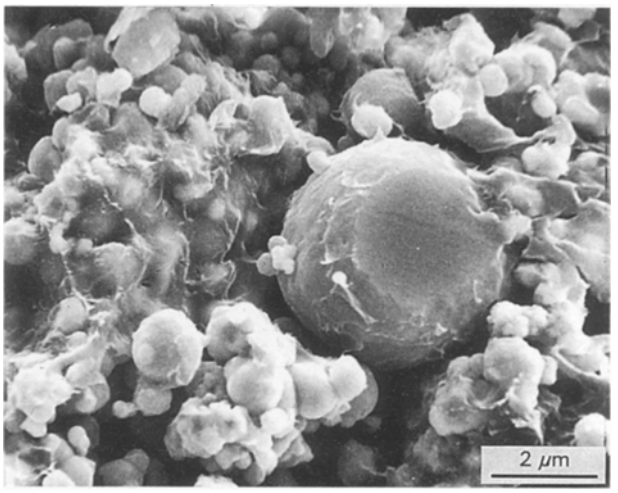

Figure 18 Scanning electron micrograph of a part at the beginning of debinding in wick and nitrogen.

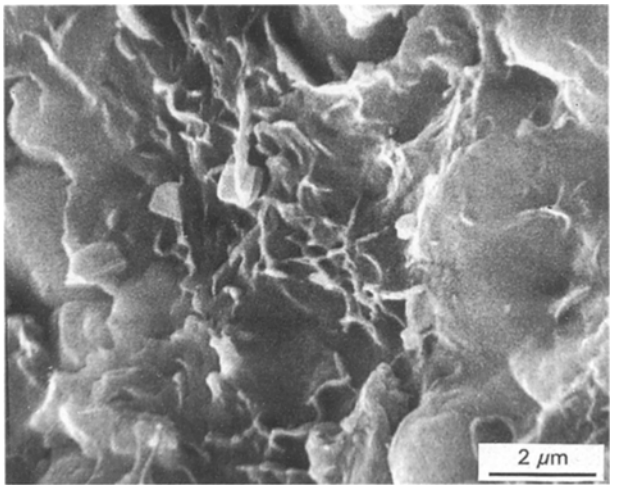

Figure 19 Scanning electron micrograph of a part at the beginning of debinding in wick and nitrogen.

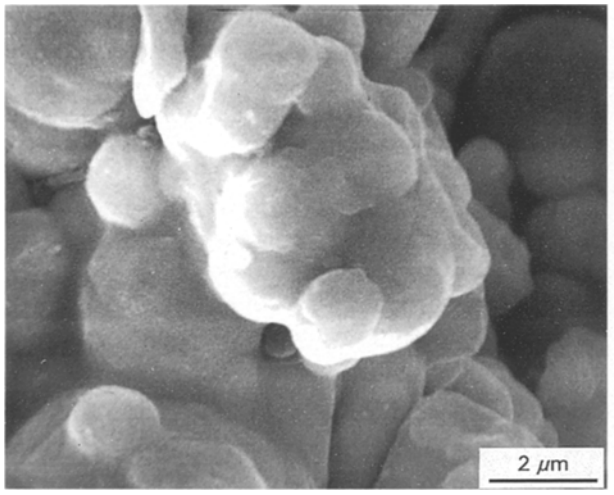

Figure 20 Scanning electron micrograph of a part 25% debound in wick and nitrogen.

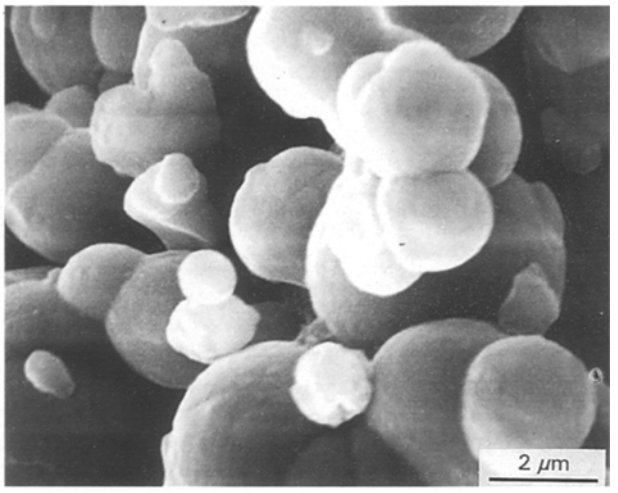

Figure 22 Scanning electron micrograph of a part 80% debound in wick and nitrogen.

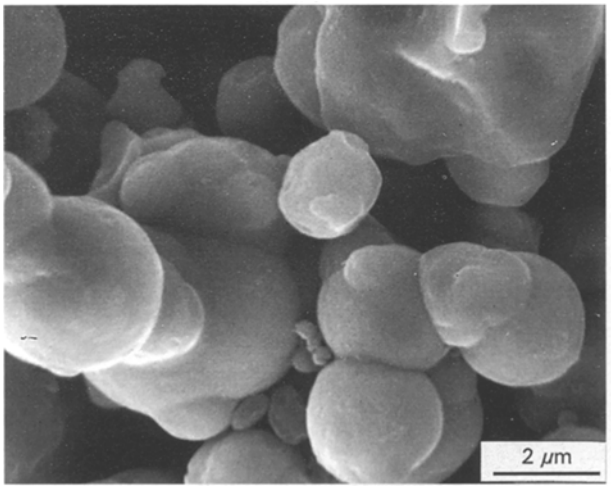

Figure 21 Scanning electron micrograph of a part 25% debound in wick and nitrogen with a small pore channel developing.

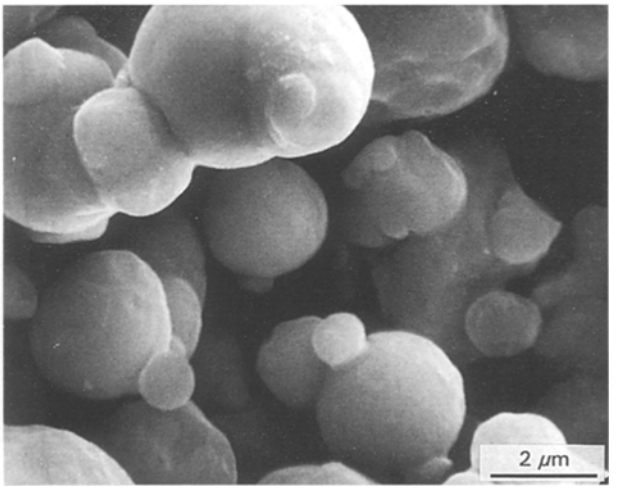

Figure 23 Scanning electron micrograph of a part 80% debound in wick and nitrogen, demonstrating pendular bonds between two particles.

demonstrating that the process of developing an interconnected channel system has begun. As debinding proceeds, the amount of binder removed and the pore volume continue to increase. Figs 22 and 23 show the centre region of the sample after 8 h debinding, when 80% of the binder is removed. Small amounts of binder can still be observed. Some powders, however, are not surrounded by binder except at contact points between particles where they form pendular bonds, as demonstrated in Fig. 23.

The process of removing the multicomponent binder applied in this work can be described as a sequence of the following stages: first, at relatively low temperatures, low melting point binders (in this work paraffin and *Carnauba* waxes) soften, melt and begin to flow out of the compact. At this stage binder removal is assisted by capillary forces introduced by the presence of wick powder. They draw liquid waxes into smaller pores at the surface and speed up the formation of small interconnected pore channels in the compact, as shown in Fig. 20.

As debinding proceeds, binders begin to decompose and vaporize. Because the pore diameters of the created channels are very small, the diffusion rate of the decomposed gas is quite slow. To avoid cracks and bubbles that can easily develop if the diffusion rate is slower than the gas formation rate, the debinding time at low temperatures should be kept reasonably long before the temperature is raised to a higher level, where the decomposition rate of the binders is fast. This approach was also applied, as shown by the temperature profile in Fig. 17.

As debinding proceeds, these fine pore channels open up and allow volatile products to diffuse through and escape to the ambient. The average pore size shifts to a small magnitude, but the amount of pores increases. With increasing debinding temperature, binders become less viscous and are forced to the surface by internal gas pressure. A structure of powder–binder agglomerates and large interparticle voids is created. These large pore channels induced by temperature rise accelerate the debinding rate, as shown by the TGA and the DTGA curves in Figs 10 and 11, respectively.

As debinding continues at higher temperatures, only small amounts of binder are left at contact points between particles, as shown in Fig. 23. These can be removed during a subsequent sintering process.

4. Conclusions

The process of removing a multicomponent binder, consisting of LMW polyethylene, paraffin and *Carnauba* waxes, from an iron–aluminium powder compact was investigated. Plastisol formulation (63 vol% metal powder content) was optimized using rheological measurements (viscosity).

The debinding experiment using heat and fluid wicking, demonstrated the following points.

1. Thermal debinding in air produced an oxidized sample with many defects.
2. Thermal debinding in nitrogen resulted in total removal of the binder after approximately 8 h and left a slightly warped sample.
3. Debinding by means of fluid wicking removed no more than 30% of the binder and can be used only as the first step in the debinding process, to open up small channels by capillary forces and to facilitate the further thermally activated process; the time dependence of fractional debinding, $x(t)$, during wicking has been estimated using a model.
4. The wick-assisted thermal debinding in the protective atmosphere of nitrogen proved to be an effective debinding method in terms of shape preservation and the absence of defects in the studied material.

Direct SEM observations were made on samples at different stages of wick-assisted thermal debinding in nitrogen, monitoring the binder distribution and the pore-structure evolution during the process. It was found that first the sample was fully filled with binder, then binder and particles form discrete islands of agglomerates with small interconnected pore channels and, at the final stage, regions where only small amounts of binder are present form pendular bonds at the contact points between particles, holding these particles together.

Because the metal powder system applied in this work is typical of injection moulding morphology, the debinding results presented here can be treated as guidelines and extrapolated to other compositions having the same morphological characteristics.

Acknowledgement

Financial support by IOP-Metals (Innovative Research Programme) is gratefully acknowledged.

References

1. P. CALVERT and M. CIMA, *J. Am. Ceram. Soc.* **73** (1990) 575.
2. G. C. STANGLE and I. A. AKSAY, *Chem. Eng. Sci.* **45** (1990) 1719.
3. J. R. GASPEROVICH and R. C. DREWES, *Int. J. Powder Metall.* **27**(2) (1991) 169.
4. S. T. LIN and R. M. GERMAN, *Powder Metall. Int.* **21**(5) (1989) 10.
5. C. W. FINN, *Int. J. Powder Metall.* **27**(2) (1991) 127.
6. K. S. HWANG and K. H. LIN, *ibid.* **28**(4) (1992) 357.
7. H. H. ANGERMANN, F. K. YANG and VAN DER BIEST, *J. Mater. Sci.* **27** (1992) 2534.
8. C. G. McKAMEY, J. H. DeVAN, P. F. TORTORELLI and V. K. SIKKA, *J. Mater. Res.* **6** (1991) 1779.
9. R. M. GERMAN, "Powder Injection Molding" (Metal Powder Industries Federation, Princetown, NJ, 1990).
10. K. F. HENS, in "Proceedings of the Intensive course on MIM", Technical University Delft, The Netherlands (1992) p. 3-1.
11. M. VOGEL, "Nichtmetalle in Metallen" (D. Hischfeld, Munster, Deutche Gesellschaft fur Metallkunde, Oberursel, 1987) p. 197.
12. I. MAJEWSKA-GLABUS, "Plastisol formulation with Fe_3Al–X intermetallics for injection moulding", Technical report, Delft University of Technology, Laboratory for Material Science. Delft, The Netherlands (1990).
13. I. MAJEWSKA-GLABUS, L. ZHUANG, R. VETTER and J. DUSZCZYK, in "Proceedings of High Temperature Intermetallics" (The Royal Society, London, 1991) p. 162.
14. H. ZHANG, R. M. GERMAN and A. BOSE, *Int. J. Powder Metall.* **26**(3) (1990) 217.
15. K. F. HENS, S. T. LIN, R. M. GERMAN and D. LEE, *J. Metals* **41**(8) (1989) 17.
16. M. SANDERS, Master Thesis, Delft University of Technology, Delft, The Netherlands (1991).
17. R. M. GERMAN, *Int. J. Powder Metall.* **23**(4) (1987) 237.
18. R. VETTER, M. SANDERS, I. MAJEWSKA-GLABUS, L. Z. ZHUANG and J. DUSZCZYK, *J. Powder Metall.*, in press.

Received 4 January
and accepted 15 March 1995